Application of the Sinc Basis Moment Method to the Reconstruction of Infinite Circular Cylinders

THOMAS J. CAVICCHI, STEVEN A. JOHNSON, AND
WILLIAM D. O'BRIEN, JR., MEMBER, IEEE

Abstract—**A solution of the ultrasonic scattering and inverse scattering problem has been obtained by solving the inhomogeneous Helmholtz wave equation via the sinc basis moment method. In this numerical study the algorithm of Johnson and Tracy has been applied to the reconstruction of an infinite circular cylinder that is subject to an incident cylindrical wave of ultrasound and is surrounded by a homogeneous coupling medium. For weak scattering cylinders, successful reconstructions have been obtained using the known exact solution for the scattered field as the input data for the algorithm. Five-percent noise added to the scattered field values does not significantly affect performance. A detailed discussion of sampling requirements for this algorithm is presented, and the threshold derived correlates well with results of a numerical study of variation of the sampling density. Effects of varying object contrast, object size, grid size, sampling density, and method of iteration are investigated. Optimization of computation is described, for slowness is the most serious limitation of the algorithm. Use of either the discrete scattered field equations or the exact Bessel function series solution yielded identical results, verifying the validity of the sinc function expansions.**

I. Introduction

In a recent series of papers [5], [6], [12] discrete/numerical solutions of the ultrasonic scattering and inverse scattering problem, described by the exact inhomogeneous Helmholtz wave equation were presented. Perturbation approximations were not introduced. Although for a given density of sampling there are still limitations on the degree of contrast of an object for which the solution algorithm converges, the reconstructions are much better than those of the first Born approximation.

In this computational study, effects of varying the sampling density, object contrast and radius, object grid size, and iteration duration are investigated. First, Johnson and Tracy's [5] formulation and solution algorithm are restated. Miscellaneous programming details and issues are discussed next. In particular, the topics of scattered field generation and sampling are examined. Finally, a summary of computational results presented in Section IV indicates the utility of their algorithm for solving small inverse scattering problems, and the effects of varying certain parameters. The specific case of an infinite circular cylindrical object is considered.

Manuscript received June 13, 1986; accepted December 15, 1986.

This work supported in part by the NIH Radiation Oncology Training Fellowship CA 09067, and in part by NIH CA 36029 at the University of Illinois, and in part by NIH HL 34995 and NIH CA 29728, both at the University of Utah.

T. J. Cavicchi and W. D. O'Brien, Jr., are with the Department of Electrical and Computer Engineering, University of Illinois, 1406 W. Green St., Urbana, IL 61801.

S. A. Johnson is with the Department of Bioengineering, University of Utah, Salt Lake City, UT 84112.

IEEE Log Number 8717144.

II. Problem Formulation

The inhomogeneous wave equation approximately describing the propagation of ultrasound in tissue is, assuming negligible spatial variation in density,

$$(\nabla^2 + k_0^2) f(\mathbf{r}) = -\gamma(\mathbf{r}) f(\mathbf{r}), \tag{1}$$

where

k_0 = wavenumber in reference medium;
= ω/c_0, where ω = radial frequency of the insonifying wave and c_0 = speed of sound in the reference medium;
$f(\mathbf{r})$ = the total ultrasonic field;
$\gamma(\mathbf{r})$ = the object function to be reconstructed from scattered field data;
= $\omega^2(1/c(\mathbf{r})^2 - 1/c_0^2) - i\omega\alpha(\mathbf{r})/c(\mathbf{r})$ where $\alpha(\mathbf{r})$ is the (spatially varying) power (twice the pressure) absorption coefficient and $c(\mathbf{r})$ is the speed of sound distribution function in the object region.

The well-known integral equation equivalent to (1) for the field $f(\mathbf{r})$ due to the interaction of the incident wave with the inhomogeneous medium is

$$f^{sc}(\mathbf{r}) = f(\mathbf{r}) - f^{inc}(\mathbf{r}) = \int_{-\infty}^{\infty}\int \gamma(\mathbf{r}') f(\mathbf{r}') \, G(|\mathbf{r} - \mathbf{r}'|) \, d\mathbf{r}' \tag{2}$$

where $f^{sc}(\mathbf{r})$ is the scattered field, $f^{inc}(\mathbf{r})$ is the incident field, and $G(\cdot)$ is the free-space Green function.

The two-dimensional inverse scattering problem (2) takes the form

$$f^{sc}(x, y) = f(x, y) - f^{inc}(x, y) = (-i/4) \int_{-\infty}^{\infty}\int \gamma(x', y') f(x', y') \cdot H_0^{(2)}\left(k_0 \sqrt{(x - x')^2 + (y - y')^2}\right) dx' \, dy' \tag{3}$$

where $(-i/4)H_0^{(2)}(k_0 r)$ is the free-space Green function in two dimensions (assuming time dependence $e^{i\omega t}$). If $\gamma(x, y) f(x, y)$ is a bandlimited function, it can be expanded over the set of sinc basis functions

$$\gamma(x, y) f(x, y) \cong \sum_a \sum_b \gamma(ah, bh) f(ah, bh) \cdot \left(\frac{\sin\{\pi(x - ah)/h\}}{\pi(x - ah)/h}\right) \cdot \left(\frac{\sin\{\pi(y - bh)/h\}}{\pi(y - bh)/h}\right) \quad (4)$$

where h is the sampling interval in both x and y directions. Substituting (4) into (3) results in the set of equations that may be used to estimate the unknown object function $\gamma(x, y)$ at the grid points $x = ah$, $y = bh$.

A useful physical configuration (Fig. 1) for this problem is a set of field detectors and transmitting transducers located outside the object region, which consists of a rectangularly sampled grid completely containing the cross section of the scattering object.

Specializing (3) with expansion of γf over the set of sinc basis functions (4) to exterior (detection) points gives

$$f_{\phi m}^{sc} = \sum_j D_{mj} \gamma_j f_{\phi j} \quad (5)$$

and to interior (object grid) points gives

$$f_{\phi \ell} = f_{\phi \ell}^{inc} + \sum_j C_{\ell j} \gamma_j f_{\phi j} \quad (6)$$

where

- ϕ = transmitter position index. $1 \le \phi \le n_{\text{trans}}$ where n_{trans} is the total number of transmitter positions. For each ϕ there are two independent sets of equations in (5) and (6);
- m = detector position index. $1 \le m < n_{\text{det}}$ where n_{det} is the number of detectors. m corresponds to location (x_m, y_m). For each ϕ in (5) there are n_{det} independent equations;
- ℓ = index of location (nh, ph) in the object region. $1 \le \ell \le N$ where N is the number of samples in the object region grid. For each ϕ in (6) there are N independent equations. ℓ and m correspond to (x, y) in (3);
- j = index of location (ah, bh) in the object region. $1 \le j \le N$. j corresponds to (x', y') in (3); and

$$D_{mj} = (-i/4) \int_{-\infty}^{\infty} \int H_0^{(2)}\left(k_0 \sqrt{(x_m - x')^2 + (y_m - y')^2}\right) \cdot \left(\frac{\sin\{\pi(x' - ah)/h\}}{\pi(x' - ah)/h}\right) \cdot \left(\frac{\sin\{\pi(y' - bh)/h\}}{\pi(y' - bh)/h}\right) dx'\, dy' \quad (7a)$$

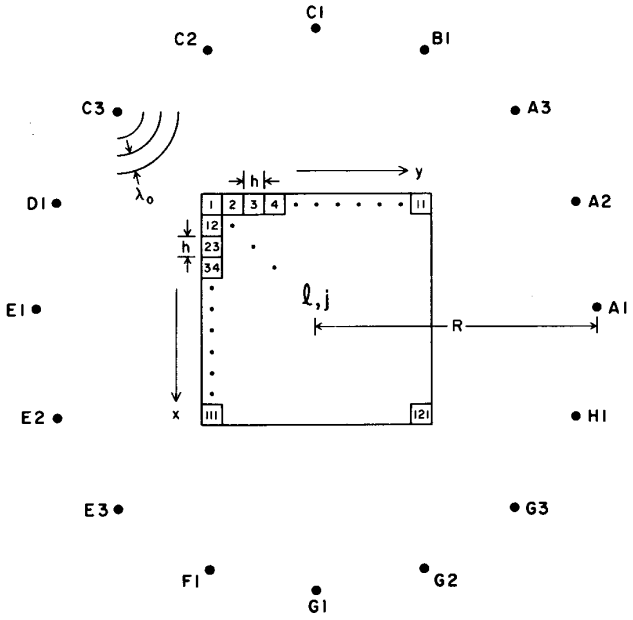

Fig. 1. Geometrical configuration of reconstruction simulations. Lettered dots situated on the circle of radius R represent line transmitting/receiving transducers. The square object region (in this case an 11×11 pixel^2 grid) is centrally located. Pixel l is at location $(x, y) = (nh, ph)$ and pixel j is at (ah, bh). λ_0 is the wavelength of the incident field, a cylindrical wave, in the coupling medium. The D coefficients in (5) and (7a) corresponding to transducers of sections B through H can be related by symmetry to those of section A.

$$C_{\ell j} = (-i/4) \int_{-\infty}^{\infty} \int H_0^{(2)}\left(k_0 \sqrt{(nh - x')^2 + (ph - y')^2}\right) \cdot \left(\frac{\sin\{\pi(x' - ah)/h\}}{\pi(x' - ah)/h}\right) \cdot \left(\frac{\sin\{\pi(y' - bh)/h\}}{\pi(y' - bh)/h}\right) dx'\, dy'. \quad (7b)$$

Many useful details for the computation of D_{mj} and $C_{\ell j}$ can be found in Tracy and Johnson [12].

In terms of the standard method of moments terminology, the basis functions are shifted sinc functions with shift argument being the location of a point in the object region in both (5) and (6). The testing functions are Dirac delta functions (point matching), where the shift argument of the delta functions is in (5) the location of a detector and in (6) the location of a point in the object region. In fact, point matching is equivalent to the discretization of the continuous integral equation in (3).

Note that in (5) and (6) there are two unknowns: f and γ. Following Johnson and Tracy's [5] algorithm a single iteration constitutes: (a) Initial guesses ($\hat{f}^0 = f^{inc}$, $\tilde{\gamma}^0 = 0$) are assigned. (b) (5) is solved for $\tilde{\gamma}^1$: by way of the algebraic reconstruction technique (ART) using scattered field data obtained as described below, holding $f = \hat{f}^0$ fixed. A version of ART was developed using [4]. (A sig-

nificant difference from previous uses of ART is that here the relevant matrices are nonsparse.) Note that (5) becomes a set of linear equations for $\tilde{\gamma}^1$. (c) Now holding $\tilde{\gamma}^1$ fixed, (6) is solved for $\tilde{f}^1$ for all ϕ. Steps (b)–(c) are repeated until convergence is obtained.

III. Programming Details

A. Incident Field

For an incident field we use a cylindrical line source (proportional to the two-dimensional free-space Green function)

$$f_{\phi j}^{\text{inc}} = H_0^{(2)}\left(k_0\sqrt{(x_\phi - ah)^2 + (y_\phi - bh)^2}\right) \quad (8)$$

where (ah, bh) = jth pixel coordinates vector and (x_ϕ, y_ϕ) = view ϕ source coordinates vector.

B. Coefficient Symmetry

It can be seen from [12] that the C_{ij} depend only on $(m - a)$ and $(p - b)$, so the number of C_{ij} coefficients that needs to be computed is only $n_{\max} \cdot (2n_{\max} - 1)$ where $n_{\max} = \sqrt{N}$, instead of $n_{\max}^4$, the total possible combinations of m, p, a, b.

Also, if n_{trans} is divisible by 8, for instance, there is symmetry in the D_{mj} coefficients. Examination of Fig. 1 reveals that all of the coefficients can be related to those in section A (receivers A1–A3), so we need calculate D_{mj} for only section A. This reduces the number that needs to be calculated from $n_{\text{det}} \cdot N$ (symmetry not accounted for) to $(n_{\text{det}}/8 + 1) \cdot N$.

C. Scattered Field Generation

Two methods are considered here.

1) In the first method, we choose a γ^{exact} to be reconstructed, and then use the reconstruction equations (5) and (6) to generate scattered field data to use as input to the reconstruction algorithm as described above. Using γ^{exact} in (6) we solve for f^{exact}. Then both γ^{exact} and f^{exact} are used in (5) to obtain f^{sc}. The problem with this method is that, while self-consistency of the algorithm may be demonstrated, the ability to reconstruct with experimental data is not ascertained.

2) The second method produces data that is mathematically closer to what ideally would be measured experimentally, and is obtained without using the sinc function expansion reconstruction equations. Here we choose as γ an object for which exact scattered data (that is, the exact solution of (1)) can be calculated. In two dimensions, the obvious choice is a cylindrically shaped object of circular cross section.

D. Sampling

This discussion of sampling involves only the interior object region; the transmitters/receivers are not constrained in this way. Care must be used in choosing the sampling interval h to avoid aliasing. By taking the Fourier transform of (2) evaluated in the object region, it is seen that the spectrum of the total field is

$$\begin{aligned}\mathcal{F}\{f(\mathbf{r})\} &= \mathcal{F}\{f^{\text{inc}}(\mathbf{r})\} + \mathcal{F}\{\gamma(\mathbf{r})f(\mathbf{r})\} \cdot \mathcal{F}\{G(r)\} \\ &= \mathcal{F}\{f^{\text{inc}}(\mathbf{r})\} + \left(\mathcal{F}\{\gamma(\mathbf{r})\} \right. \\ &\quad \left. * \mathcal{F}\{f(\mathbf{r})\}\right) \cdot \mathcal{F}\{G(r)\}. \end{aligned} \quad (9)$$

(The convolution in (9) precludes use of the spatial Fourier domain to simplify calculation of high-order solutions of (2).) In two dimensions [9]

$$\mathcal{F}\{G(r)\} = 1/(k^2 - k_0^2) - i\pi\delta(k^2 - k_0^2), \quad (10)$$

which has a singularity on the k_0 circle. A 0th order Hankel function situated far from any point in the object region has been chosen for $f^{\text{inc}}(\mathbf{r})$. Its Fourier transform therefore has a singularity on the k_0 circle and rapidly decays away from it.

$\mathcal{F}\{f(\mathbf{r})\}$ appears on both sides of (9). For a rough estimation of the bandwidth of $f(\mathbf{r})$ it is sufficient, for weak scattering, to replace $f(\mathbf{r})$ by $f^{\text{inc}}(\mathbf{r})$ on the right hand side of (9). Therefore the second term in (9) is a blurred spectrum of $\gamma(\mathbf{r})$ smeared around the $k_0 = 2\pi/\lambda$ circle and multiplied by the circularly symmetric, and singular at k_0, spectrum of $(-i/4)H_0^{(2)}(k_0 r)$. Depending on the magnitude of $\gamma(\mathbf{r})$, then, the spectrum of the total field extends out to $\Omega_{\max_f} \cong k_0 + \Omega_{\max_\gamma}$ where $\Omega_{\max_\gamma}$ is the maximum spatial frequency in γ. For a circular function of radius a,

$$\gamma(\mathbf{r}) = g(r) \triangleq \omega^2(1/c_1^2 - 1/c_0^2) \cdot \begin{cases} 1 & r \le a \\ 0 & r > a \end{cases} \quad (11)$$

where c_1 is the speed of sound in the cylinder. The Fourier transform of $\gamma(\mathbf{r})$ is

$$\begin{aligned}\mathcal{F}\{\gamma(\mathbf{r})\} = \tilde{g}(\rho) &= \omega^2(1/c_1^2 - 1/c_0^2) \\ &\quad \cdot (2\pi a^2) J_1(2\pi a\rho)/(2\pi a\rho) \end{aligned} \quad (12)$$

where ρ is the radius of the two-dimensional spatial frequency vector (units of cycles/mm) and $J_1(\cdot)$ is the first order Bessel function of the first kind. The envelope of $\tilde{g}(\rho)$ goes as $\rho^{-3/2}$. At $a\rho = 1/4$, $\tilde{g}(\rho)$ is 3 dB below its maximum value ($\tilde{g}(0) = \omega^2(1/c_1^2 - 1/c_0^2) \cdot \pi a^2$). For a cylinder discretized onto a square grid, $a = m_{\text{cyl}} \cdot h$ where m_{cyl} is the number of samples in the radius of the cylinder. Then the Fourier transform of the cylinder is 3 dB below its maximum value (at $\rho = 0$) for $\rho \ge 1/(4m_{\text{cyl}} \cdot h)$, which in units of rad/mm is $\Omega_{\max_\gamma} = \pi/(2m_{\text{cyl}} \cdot h)$.

The bandwidth of the Fourier transform of a product of two functions is the sum of the bandwidths of the individual functions. In the present case, the tails caused by $\gamma(\mathbf{r})$ in the product $\gamma(\mathbf{r})f(\mathbf{r})$ may be of substantially lower magnitude than the main component of $f(\mathbf{r})$, namely $f^{\text{inc}}(\mathbf{r})$, because of the small magnitude of $\gamma(\mathbf{r})$ dictated by how greatly c_1 differs from c_0. To avoid severe aliasing we must sample at twice the bandwidth of γf when representing γf by a sum of its samples times shifted sinc

functions. Thus, the sampling rate must satisfy

$$2\pi/h = 2\epsilon(\Omega_{\max_\gamma} + \Omega_{\max_f}) \quad (13a)$$

$$= 2\epsilon(\Omega_{\max_\gamma} + \Omega_{\max_\gamma} + 2\pi/\lambda) \quad (13b)$$

$$= 2\epsilon(\pi/(m_{\text{cyl}} \cdot h) + 2\pi/\lambda) \quad (13c)$$

or

$$h = (\lambda/2)(1/\epsilon - 1/m_{\text{cyl}}) \quad (13d)$$

where $\epsilon = 1$ for "Nyquist" sampling, $\epsilon < 1$ for undersampling, and $\epsilon > 1$ for oversampling.

Similarly, in order for the sinc function expansion of the Hankel function used in computing the $C_{\ell j}$ and D_{mj} coefficients in (5) and (6) to be valid, the same sampling rate, $2\pi/h$, must exceed twice the maximum frequency in that function: $\Omega_{\max_{H_0}}$. The Fourier transform of the zeroth order Hankel function, given above, falls 3 dB below its value at zero for $k = 1.55k_0$. Fig. 2 shows the real part of $\mathfrak{F}\{(-i/4)H_0^{(2)}(k_0 r)\}$, its -3-dB frequency, and the bandwidths of γf for $m_{\text{cyl}} = 4$ and 11. However, it is H_0^c that is expanded, a function equal to H_0 everywhere except near the origin, where the singular Y_0 component is replaced by a smooth capping function [12]. Thus the actual spectrum is likely to be much narrower than that in Fig. 2 because of the absence of the singularity, making $\Omega_{\max_{\gamma f}}$ the critical frequency in the determination of the sampling rate. Therefore $\epsilon = 1$ is a rough threshold (for the cylinder sizes considered in this study) on resulting quality of reconstructions.

If $m_{\text{cyl}} = 4$ (value for the 11×11 object region) and $\epsilon = 1$, then $h = \lambda/2.7$. For the case $m_{\text{cyl}} = 11$ (largest cylinder in this study), $h = \lambda/2.2$. It is stated in [5] that we must sample at $\lambda/4$. For the limit of an infinitely wide cylinder, in theory one could sample at $\lambda/2$. However, then the bandwidth of γf would approach the frequency of the singularity of the spectrum of $(-i/4)H_0^c$ so that its expansion over the sinc basis would now be invalid even though the expansion of γf may be valid. It therefore appears that the maximum sample spacing allowable is somewhere between $\lambda/2$ and $\lambda/4$.

It should be emphasized that the spectra of $\gamma(\mathbf{r})$, $f(\mathbf{r})$, and $(-i/4)H_0^c(k_0 r)$ all extend in both the x and y directions to infinite frequencies. Hence there is no strict Nyquist frequency. As defined here, Nyquist frequency refers to the sampling rate above which the reconstructions are predicted to be acceptable and below which the reconstructions would be poor because of severe aliasing. The -3-dB frequency was chosen as a consistent indicator at which the slopes of the spectra are steep so that small variations in the sampling rate will show large changes in the quality of the reconstructions. Of course, in the end of the simulations themselves will give the final answer. Also, for weak scattering and oversampling, the coefficients $C_{\ell j}$ and D_{mj} are problem-independent because a single sampling rate will suffice for all problems likely to be encountered.

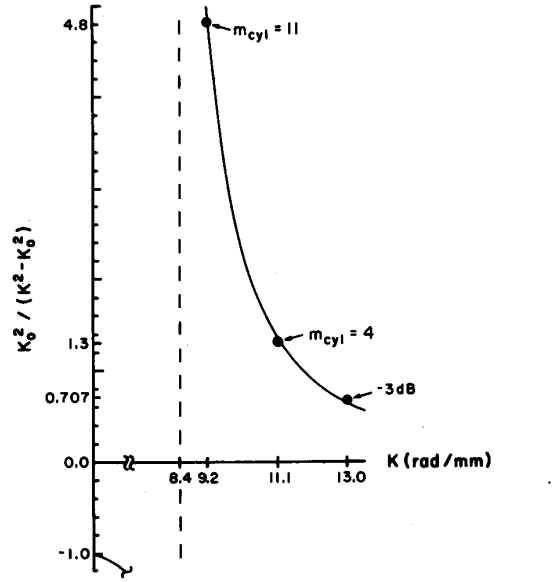

Fig. 2. k_0^2 times the real part of the Fourier transform of $(-i/4)H_0^{(2)}(k_0 r)$ where $k_0 = 8.4$ rad/mm. Points specified are -3 dB bandwidths of γf for $m_{\text{cyl}} = 11$ and 4, and the -3-dB point of $k_0^2/(k^2 - k_0^2)$. As $m_{\text{cyl}} \to \infty$, the bandwidth of γf approaches k_0, the singularity of $k_0^2/(k^2 - k_0^2)$. The -3-dB point further out (γf vs. H_0^c) must be used to determine sampling, but the smoother H_0^c is actually expanded rather than H_0, so that point may be the -3-dB point of γf.

E. Optimization of Speed of Program

Two ideas that resulted in program modification to reduce run time are discussed here. Two further improvements due to parameter selection appear in Section IV. First, if one considers solving (6) by ART-type methods, one obvious procedure is to solve the subset of equations for a particular view of the internal field for a particular source position, then do the same for the next view, etc. Although in obtaining the elements of the matrix rows (in (6) these are $C_{\ell j}\gamma_j - \delta_{\ell l}$, $\delta_{\ell j}$ the Kronekar delta function), many arithmetic operations are involved, row i is the same for each view (γ is held constant during the solution of (6)). Thus it is far more efficient to update all views with row 1 (corresponding to pixel 1), then all views with row 2, etc.

Second, in ART the correction to x_j, the jth element of the unknown $\mathbf{x}$, is

$$x_j = x_j + \beta_1(y_j - (\mathbf{x}, \mathbf{r}_i))r_{ij}/\|\mathbf{r}_i\|^2 \quad (14)$$

where y_i is the ith component of the known vector $\mathbf{y}$ in $\mathbf{y} = R\mathbf{x}$, r_{ij} is the jth element of $\mathbf{r}_i$, the ith row of matrix R, and β_1 is a chosen scaling parameter. It has been found that all $\|\mathbf{r}_i\|$ are practically equal, so in the solution of (5) one can use $\|\mathbf{r}_1\|$ for all i. Furthermore, in the solution of (6) equally good results were obtained by using the simpler correction

$$x_i = x_i + \beta_0(y_i - (\mathbf{x}, \mathbf{r}_i)) \quad (15)$$

where β_0 is a chosen constant. In (15) note the simpler error scaling and the subscript i on x indicating that for

row i it is sufficient to correct only the ith element of $\mathbf{x}$, whereas it was found that for solving (5) all elements of $\mathbf{x}$ must be corrected for each row i (see (14)). These simplifications cut the run time in half.

IV. Fractional Degree of Overdetermination

To reduce the deteriorating effects of measurement noise and ill-conditioning, either n_{trans} or n_{det} can be increased. If the relevant matrix (see (5)) is well conditioned (of rank $\sim N$), then we can have $\sim N$ independent measurement equations because the field at every pixel makes a contribution to the scattered field at any point in space. Consequently, to obtain all the unique data and not overdetermine the system, $n_{\text{trans}} \cdot n_{\text{det}}$ would be set equal to N.

The optimal ratio of n_{trans} to n_{det} is about one-to-one because if xy is fixed, $x + y$ is minimized if $x = y$. Therefore, in this study n_{det} was chosen to be the lowest multiple of 8 greater than $\sqrt{N}$ and n_{trans} was then chosen as N/n_{det} times the overdetermination factor, plus one.

Two measures of fractional overdetermination (Q_1 and Q_2) may be defined. The first, describing the overdetermination for the entire system, compares the number of measurements to the total number of unknowns (in both (5) and (6)).

$$Q_1 = \left(n_{\text{trans}} \cdot n_{\text{det}} + n_{\text{trans}} \cdot N - (1 + n_{\text{trans}}) \cdot N\right)/\left[(1 + n_{\text{trans}}) \cdot N\right] = \frac{n_{\text{trans}} \cdot n_{\text{det}}/N - 1}{1 + n_{\text{trans}}} \tag{16}$$

where $n_{\text{trans}} \cdot n_{\text{det}}$ is the number of measurements, $n_{\text{trans}} \cdot N$ is the number of constraint equations (6) and $(1 + n_{\text{trans}}) \cdot N$ is the total number of unknowns. Note that Q_1 does not increase as n_{trans} (the number of views) gets large. For a fixed n_{det}, as n_{trans} gets large, Q_1 approaches n_{det}/N. Above, we found a reasonable choice for $n_{\text{det}} = \sqrt{N} = n_{\max}$. In any case, for a fixed n_{trans} clearly n_{det} will increase as $n_{\max}$. Thus as n_{trans} becomes large, Q_1 approaches the maximum of the order $1/n_{\max}$; the overdetermination Q_1 declines with grid size. But then Q_1 can not also be an indicator of resulting performance, because in Section IVC results are shown indicating that by solving exactly the same cylindrical object reconstruction problem using different sized grids, convergence appears to be practically independent of $n_{\max}$.

The other measure of fractional overdetermination is (consideration of (5) only):

$$Q_2 = n_{\text{trans}} \cdot n_{\text{det}}/N - 1 \tag{17}$$

where N represents the N unknown γ values in (5). Q_2 may actually be a more useful parameter than Q_1; we are assuming no (low) noise in our constraint equations, except that introduced via the estimated γ, which in turn is determined by the scattered field measurements via the solution of (5). The incident field, in the constraint equations, can be determined to arbitrary accuracy. Thus the correction by overdetermination for the greatest source of noise—that present in the measurements of the scattered field—is better represented by Q_2.

Choosing n_{det} and n_{trans} as described above, for $n_{\max} = 11$ they both turned out to be 16, where for all grid sizes considered Q_2 was held constant at 1.2. For comparison in [12], $n_{\text{det}} = n_{\text{trans}} = 17$ so that $Q_2 = 1.4$. Of course, if we already are aware of the symmetry of the circular cylinder, we can reduce the number of equations and obtain satisfactory results. But for a general object, they found improvement for up to 300-percent overdetermination.

V. Computational Results

In this section, results of computer simulations using the sinc basis moment method inverse scattering algorithm [5] are presented. Two types of object distribution were reconstructed: a Gaussian profile infinite cylinder and a circular infinite cylinder. The purpose of the former is to relate results of the present study to those of [12] and the purpose of the latter is to apply to algorithm to a situation for which exact scattered field data is available for the computer simulations.

The topics to be briefly discussed here include the effects of varying several parameters of the tomography-scattering object system and a few computational issues with reference to actual program runs.

For all runs, the initial guess for both the real and imaginary parts of γ was zero, c_0 was held at 1.5 mm/μsec, the frequency was 2 MHz, and the transducer–object region center distance, R, was 10λ. Except where otherwise stated, the sampling rate scale, ϵ, was about 1.5, the level of noise added to the scattered field data was 5 percent, and for circular cylinder reconstructions the number of samples across the radius of the cylinder, m_{cyl}, was $2/3 \cdot (n_{\max}/2 + 1)$ (so that the cylinder nearly fills up the object region—a condition for which $\epsilon = 1.5$ dictates cylinder radius a to be approximately λ for the 11×11 object region grid and 2λ for the 25×25 grid).

A. Scattered Field Generation

It was found that using (5) and (6) to generate the scattered field gave essentially identical reconstructions to those obtained using the "exact" equations for the circular infinite cylinder case. This is a satisfying result, for it shows that (5) and (6) are very good approximations to the corresponding exact integral equations.

B. Test: Gaussian Object

Exactly the same two-dimensional 11×11 object distribution as that reconstructed by [12] was reconstructed on our version of their algorithm. Their computation time on a PDP11/34A computer (with floating point processor) required 7 h with 2-percent noise added to the data. On our VAX 11/730 (1 Mbyte with floating point accelerator) it took, for generation of scattered field plus reconstruction, 8 min, while for reconstruction only (read in the scattered field) only 4 min (three complete iterations),

to obtain a reconstruction with slightly less error $\|\tilde{\gamma} - \gamma^{\text{exact}}\|^2$ and virtually identical appearance to the one in [12]. Here it was found that no significant degradation occurred for additive noise in the scattered field data up to 10 percent. It should be noted that the present implementation does not include the low-pass filter constraint operation referred to and applied in [5].

C. Object Contrast

In Fig. 3 an example is shown, for a 25 × 25 grid, of the reconstruction of speed of sound and absorption distributions for a 5 percent contrast, $k_0a = 13.6$ circular cylinder after four iterations. For the remaining reconstructions in this paper, only center-line profiles are included, as they are more quantitative than are the perspective views because of the possibility of using labeled axes. Also, for Fig. 3(b) and all subsequent plots in this paper, straight lines have been drawn between points (representing either pixel values or results of entire reconstructions); points have been left out for clarity.

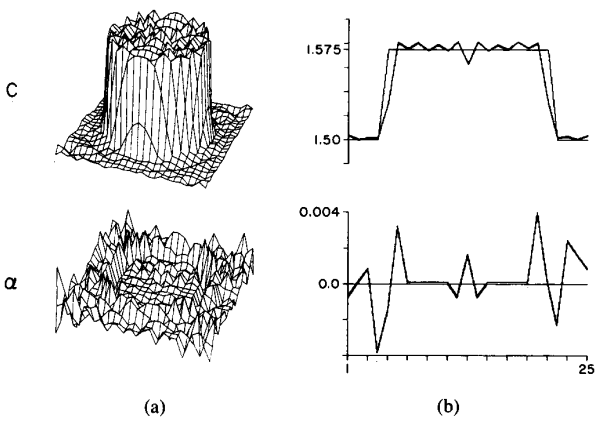

Fig. 3. Lossless circular cylindrical object reconstructions after four iterations; speed of sound (above, mm/μsec) and absorption (below, rad/mm) for 5-percent object contrast, $m_{\text{cyl}} = 8$, $n_{\max} = 25$, $k_0a = 13.6$, freq = 2 MHz, sampling rate: $\epsilon = 1.5$ in (13d). (a) perspective view (b) center line profile; here the exact solution is also plotted, with lighter line.

Good reconstructions were obtained for cylindrical objects in which the speed of sound, c_1, was different from c_0 by less than about 5 percent. Fig. 4 is a composite showing reconstructions (heavy line) against the exact solution (lighter line) for a range of −10 percent to 10 percent for three sizes of object radius. These sizes were defined by choosing $m_{\text{cyl}} = 2/3 \cdot (n_{\max}/2 + 1)$ for $n_{\max} =$ 11, 17, and 25. Looking within one column pair, one sees the dependence of reconstruction quality of speed of sound and absorption distributions upon percent object contrast for a given object radius. Within one plot, the results of both the first iteration and the fourth iteration are included. It is evident that the fourth iteration is significantly better than the first iteration, which is the Born approximation. For the first iteration the reconstructed speed of sound within the cylinder is typically too close to c_0, while in the fourth iteration it oscillates about the exact solution. This "lost energy" in the real part of γ is mixed into the imaginary part, as evidenced by the erroneous cylinder shape in the reconstructed absorption distribution (which should be zero everywhere). This effect is also evident in Soumekh and Kaveh's [11] reconstructions obtained using the Born approximation but a different method of solution. Again, in the fourth iteration the reconstructed absorption distribution oscillates about the exact solution, zero.

Beyond ±5-percent contrast in this implementation, convergence quality exponentially deteriorates (see Fig. 5), although in Fig. 4 the error in the fourth iteration exceeded that in the first for only one case: reconstruction of absorption; −10-percent contrast, 25 × 25 grid. In all other cases, the line closer to the exact solution is iteration 4. All of the results in Fig. 4 are plotted on a single graph in Fig. 5, where here the abscissa is γ (not percent contrast). The ordinate is the log of the normalized error, defined as follows. The number of pixels for which $\gamma \neq 0$ is called $n_{\gamma \neq 0}$. (Although in practice $n_{\gamma \neq 0}$ would not be known beforehand, it could be approximated by N; but because it is known here and helps to accurately characterize $\gamma(\mathbf{r})$, it is used in this paper.) The normalized error is then the sum of the squares of $\tilde{\gamma}_j - \gamma_j^{\text{ex}}$, divided by $n_{\gamma \neq 0}$.

Table I shows the results of varying object contrast of the cylinder; it contains data about all the reconstructions in Fig. 4 and some additional runs. In Table I, the characteristics given for each run include percent contrast, c_1, the squared norm of γ divided by $n_{\gamma \neq 0}$, the sum of squares of the error in γ for iterations 0 (iteration 0 is before any correction, so $\tilde{\gamma}$ is the initial guess: zero), 1, and 4, the sum of squares of the error in iteration 4 divided by $n_{\gamma \neq 0}$, the improvement factor over the Born approximation, that is, iter 0/iter 4, and the percent error in the average value of the reconstructed c_1 within the cylinder. A few examples of equal norm of γ for positive and negative contrasts are included; for example, −13.3 percent can be compared to +22 percent, −10 percent to +14.3 percent, etc. Each of these runs corresponds to a single point on one of the curves in Fig. 5. A striking feature of this table is the extremely low percentage of error in the average speed of sound in the cylinder: less than one percent error for object contrast magnitudes of less than 10 percent for all object sizes considered, and less than 0.1 percent for contrast magnitudes of less than or equal to 5 percent. One conclusion to be drawn here is that the maximum speed of sound in the cylinder for which successful reconstruction is possible declines with the object size, which varies for different m_{cyl}. It should be mentioned, however, that in soft tissue the percent contrasts are entirely within these limits for these small object sizes, and the sharp edge of the cylinder function reconstructed here mimicks well the boundaries found in tissue, such as blood vessels. Thus it may be possible, using larger grid sizes, to successfully reconstruct tissue objects of more practical sizes than those considered here.

The dependence of convergence on $n_{\max}$ for reconstruc-

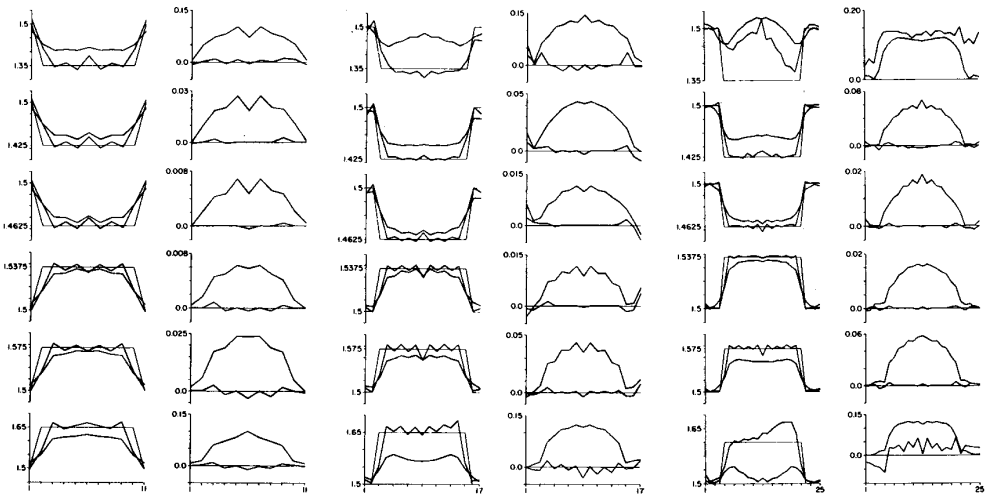

(a) (b) (c)

Fig. 4. Lossless circular cylindrical object reconstructions. Dependence of reconstruction quality of speed of sound (left column of a pair, mm/μsec) and absorption (right column of a pair, rad/mm) object contrast is shown for three object (and grid) sizes. First and fourth iterations are boldface, exact solution lighter line. In all cases except the absorption reconstruction for -10-percent contrast, $n_{max} = 25$, fourth iteration is the line closer to the exact solution. $m_{cyl} = 2/3 \cdot (n_{max}/2 + 1)$, freq = 2 MHz, sampling rate: $\epsilon = 1.5$ in (13d). From top to bottom, percent contrasts are -10 percent, -5 percent, -2.5 percent, 2.5 percent, 5 percent, 10 percent. (A) $m_{cyl} = 4$, $n_{max} = 11$, $k_0 a = 5.8$. (B) $m_{cyl} = 6$, $n_{max} = 17$, $k_0 a = 9.7$. (C) $m_{cyl} = 8$, $n_{max} = 25$, $k_0 a = 13.6$.

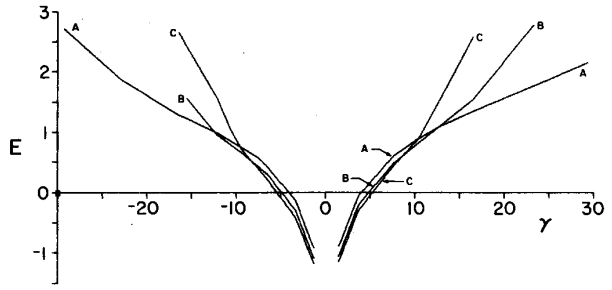

Fig. 5. Plot of log of normalized reconstruction error (sum of squares of $\tilde{\gamma}_j - \gamma_j^{ex}$ divided by $n_{\gamma \neq 0}$), E, after four iterations vs. γ (lossless cylinder, so γ is real, (rad/mm)^2). (A) $n_{max} = 11$, (B) $n_{max} = 17$, (C) $n_{max} = 25$.

tion of identical objects was earlier denied. Table II demonstrates this for three values of object contrast within otherwise identical cylinders. The same reconstruction performed on both the 11×11 and 25×25 grids yielded equivalent results, which are characterized similarly to those in Table I.

The limitation concerning object contrast appears to arise from at least two factors. The first is the somewhat inefficient procedure of holding one of the two multiplied unknowns constant while iterating only upon the other and vice-versa; if the initial guess is too far off then there may be difficulty in getting "on track." This phenomenon may be similar in effect to the difficulty encountered in the calculation of higher order terms of the Born Series [10]. This difficulty may be circumvented by further developments in the algorithm as, for example, indicated in [5].

Convergence is obtainable for greater positive percent contrasts than negative percent contrasts. However, it must also be recognized that the value of γ is asymmetric with respect to c_1/c_0: $\gamma_{cyl} = \omega^2(1/c_1^2 - 1/c_0^2)$ so that γ^2 is larger for a given negative-percent contrast than the corresponding positive-percent contrast. This consideration leads to the second factor that may be the root of the problem: the norm (or sum of the squares of the samples) of γ. We can raise the maximum speed of sound value in the Gaussian object in [12] higher than the maximum in a cylindrical object with $m_{cyl} = 2/3 \cdot (n_{max}/2 + 1)$ and still obtain convergence, because $\Sigma_j \gamma_{gauss_j}^2$ will be less than $\Sigma_j \gamma_{cyl_j}^2$ due to the Gaussian drop-off. In fact, for the cylinder having (uniform) speed of sound equal to that at the center of Tracy and Johnson's Gaussian, the reconstruction error after four iterations was over two orders of magnitude higher than that of the Gaussian. This is a greater difference than one would predict on the basis of the Gaussian being a smoother function (narrower bandwidth) than the cylinder. The advantage of considering $\|\gamma\|$ rather than c_1 in discussions of convergence is also evident in Fig. 5, which exhibits a much higher degree of symmetry about the abscissa (γ) than does a similar graph with percent contrast on the abscissa. Thus a likely cause of convergence difficulty is that when using ART to solve large, nonsparse matrices, convergence degrades with the norm of the unknown.

TABLE I
CHARACTERISTICS OF COMPUTER SIMULATIONS OF RECONSTRUCTION OF CIRCULAR CYLINDER. OBJECT CONTRAST [SAMPLING RATE: $\epsilon = 1.5$, $m_{cyl} = 2/3(n_{max} + 1)$].

	Percent Contrast	c_1 mm/μs	$\frac{\|\gamma\|^2}{n_{\gamma\neq 0}}$	Sum of Squares of $\tilde{\gamma}_j - \gamma_j$ iter 0	iter 1	iter 4	$\frac{\text{iter 4}}{n_{\gamma\neq 0}}$	$\frac{\text{iter 0}}{\text{iter 4}}$	$\bar{c}_1$ error percent
	−16.0	1.26	857	40300	35600	6850	146.	5.9	−0.21
	−13.3	1.30	540	25400	17300	2760	59.	9.2	−0.067
	−10.0	1.35	271	12740	5770	1050	22.	12.1	0.095
	−8.0	1.38	162	7620	2570	580	12.3	13.1	0.059
	−6.7	1.40	108	5070	1380	370	7.87	13.7	0.039
	−5.0	1.425	57	2700	560	190	4.	14.2	−0.0044
	−2.5	1.4625	13	620	90	40	0.85	15.5	0.0038
11 × 11	−1.0	1.485	2.0	95	12	6	0.13	15.8	0.0008
$m_{cyl} = 4$	1.0	1.515	1.9	90	10	5.7	0.12	15.9	0.0023
$n_{\gamma\neq 0} = 47$	2.5	1.5375	11	540	68	34	0.72	15.9	0.014
$k_0a = 5.78$	5.0	1.575	43	2000	330	120	2.6	16.7	0.067
	5.9	1.588	57	2700	500	170	3.6	15.9	0.10
	7.5	1.6125	89	4200	970	260	5.5	16.1	0.17
	10.0	1.65	148	6970	2190	450	9.6	15.5	0.34
	13.3	1.7	241	11350	5000	780	17.	14.6	0.79
	14.3	1.715	272	12790	6140	915	19.	14.0	1.0
	22.0	1.83	530	24900	19540	3690	79.	6.7	1.83
	31.0	1.965	857	40300	42800	24150	514.	1.7	−8.14
	−13.3	1.30	550	61100	65860	65990	595.	0.93	8.45
	−10.0	1.35	271	30080	24600	3890	35.	7.73	−0.19
	−6.7	1.40	108	11970	5420	730	6.6	16.4	0.170
	−5.0	1.425	57	6380	1960	330	3.0	19.3	0.084
17 × 17	−2.5	1.4625	13	1480	230	68	0.61	21.8	0.027
$m_{cyl} = 6$	−1.0	1.485	2.1	230	26	10	0.09	23.	0.0064
$n_{\gamma\neq 0} = 111$	1.0	1.515	1.9	212	13	9	0.081	23.6	−0.0018
$k_0a = 9.7$	2.5	1.5375	11	1270	180	55	0.49	23.1	0.0092
	5.0	1.575	43	4730	1210	215	1.94	22.	0.084
	7.5	1.6125	89	9916	4130	500	4.52	19.8	0.234
	10.0	1.65	148	16470	9920	1020	9.19	16.1	0.58
	13.3	1.70	242	26810	22870	3930	35.4	6.82	1.29
	−10.0	1.35	271	53400	64630	73390	373.	0.73	5.7
	−8.0	1.38	162	31960	29030	6610	33.6	4.8	−0.85
	−6.7	1.40	108	21240	14740	1520	7.7	14.	−0.2
	−5.0	1.425	58	11330	5040	520	2.6	22.	0.09
	−2.5	1.4625	13	2620	450	96	0.49	27.3	0.033
25 × 25	−1.0	1.485	2.0	400	37	14	0.07	28.6	0.01
$m_{cyl} = 8$	1.0	1.515	1.9	380	33	13	0.07	29.2	0.008
$n_{\gamma\neq 0} = 197$	2.5	1.5375	11	2250	350	75	0.38	30.0	−0.012
$k_0a = 13.57$	5.0	1.575	43	8390	3120	313	1.6	27.	0.05
	7.5	1.6125	89	17600	11550	1030	5.2	17.1	0.065
	8.5	1.6275	111	21990	17030	2090	10.6	10.5	1.09
	10.0	1.65	148	29230	27620	7260	37.	4.0	1.0
	−14.3	1.715	272	53590	71270	87550	444.	0.61	13.

[a] Parameters varied: speed of sound within the cylinder, c_1 (object contrast). See text for definition of all parameters.

TABLE II
CHARACTERISTICS OF COMPUTER SIMULATIONS OF RECONSTRUCTION OF CIRCULAR CYLINDERS GRID SIZE (SAMPLING RATE $\epsilon = 1.5$, $m_{cyl} = 4$, $k_0a = 5.78$, $n_{\gamma\neq 0} = 47$)[a]

Percent Cont.	c_1 mm/μs	n_{max}	$\frac{\|\gamma\|^2}{n_{\gamma\neq 0}}$	Sum of Squares of $\tilde{\gamma}_j - \gamma_j$ iter 0	iter 1	iter 4	$\frac{\text{iter 4}}{n_{\gamma\neq 0}}$	$\frac{\text{iter 0}}{\text{iter 4}}$	$\bar{c}_1$ Error (percent)
−10.0	1.35	11	271	12740	5770	1050	22.0	12.1	0.095
−10.0	1.35	25	271	12740	5690	1140	24.0	11.2	0.015
−5.0	1.425	11	57	2700	560	190	4.0	14.2	−0.0044
−5.0	1.425	25	57	2700	570	196	4.2	13.8	0.0038
10.0	1.65	11	148	6970	2190	450	9.6	15.5	0.34
10.0	1.65	25	148	6970	2190	470	9.9	14.8	0.49

[a] Parameters varied: n_{max} (grid size). See text for definition of all parameters.

TABLE III
CHARACTERISTICS OF COMPUTER SIMULATIONS OF RECONSTRUCTION OF CIRCULAR CYLINDERS. OBJECT RADIUS (25 × 25 GRID, −5 PERCENT CONTRAST, SAMPLING RATE: $\epsilon = 1.5$).

$n_{\gamma\neq 0}$	m_{cyl}	k_0a	$\frac{\|\gamma\|^2}{n_{\gamma\neq 0}}$	Sum of Squares of $\tilde{\gamma}_j - \gamma_j$			$\frac{\text{iter 4}}{n_{\gamma\neq 0}}$	$\frac{\text{iter 0}}{\text{iter 4}}$	$\bar{c}_1$ Error (percent)
				iter 0	iter 1	iter 4			
47	4	5.78	57.4	2700	680	200	4.3	13.5	0.03
102	6	10.1	62.5	6380	1970	300	2.9	21.3	0.062
197	8	13.6	57.5	11330	5040	520	2.6	21.8	0.09
376	11	18.9	57.3	21560	15330	1370	3.6	15.7	0.15

[a] Parameter varied: m_{cyl} (object radius). See text for definition of all parameters.

D. Object Size

In the previous subsection, $\|\gamma\|$ increased for increasing speed of sound contrast, while within one column pair of Fig. 4 $n_{\gamma\neq 0}$ remained constant. Actually, in the study of reconstruction of circular cylinders, the parameter best correlating (inversely) with quality of reconstructions seems to be $\|\gamma\|^2/n_{\gamma\neq 0}$. Changing object size for a given contrast increases both $\|\gamma\|$ and $n_{\gamma\neq 0}$ so that $\|\gamma\|^2/n_{\gamma\neq 0}$ remains constant. It was found that when the object contrast was held constant and the cylinder radius was increased from 0.9λ to 3.0λ, the reconstruction quality remained about the same (see Fig. 6). Note in the $k_0a = 18.9$ object that the reconstruction is somewhat smoother than those of the smaller objects. At least two competing trends are present when increasing the cylinder radius: the discretized cylinder shape approaches more closely the smooth circle of a continuous cylinder while the sampling (for constant ϵ) approaches the singularity of $\mathfrak{F}\{(-i/4)H_0^c\}$ at k_0.

Table III summarizes the reconstruction results for the study of varying the object radius as shown in Fig. 6. Here the first three columns are $n_{\gamma\neq 0}$, m_{cyl}, and k_0a; otherwise the same result characteristics are given here as in Tables I and II. The above statement that the quality of reconstruction is relatively constant for the investigated sizes of cylinders is evident by examining the improvement factor defined earlier which, however, is beginning to decline for the largest cylinder, $k_0a = 18.9$. Also, $\|\gamma\|^2/n_{\gamma\neq 0}$ is essentially constant for all sizes considered, as indicated above, while in Tables I and II that ratio varied inversely with reconstruction quality.

One can also view in Fig. 5 how increasing object size by a factor of 2.3 affects the dependence of convergence on $\|\gamma\|$. While for low contrast cylinders the error after four iterations is lowest for the largest cylinder, the opposite is true when $|\gamma| > 10\ (\text{rad/mm})^2$ (that is, object contrast greater than about 8 percent and less than −7 percent). Thus, while for larger objects the maximum contrast allowable for successful reconstruction declines, the performance for low contrast objects is actually slightly better.

E. Sampling

The numerical consequences of the earlier discussion on sampling are evident in Fig. 7. Holding everything else

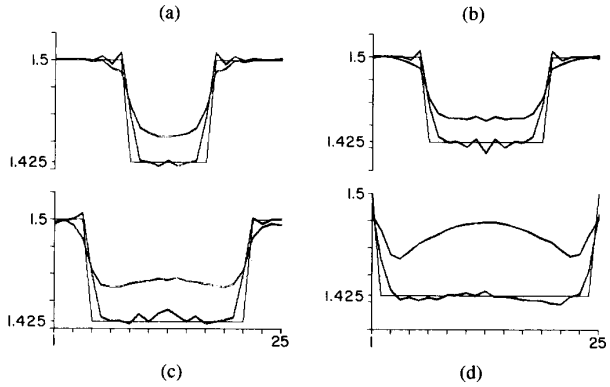

Fig. 6. Circular cylindrical object reconstructions. Dependence of reconstruction quality of speed of sound (mm/μsec) on object radius is shown for the 25 × 25 pixel² grid. Freq. = 2 MHz, sampling rate: $\epsilon = 1.5$ in (13d), object contrast = −5 percent. (a) $m_{cyl} = 4$, $k_0a = 5.8$ (b) $m_{cyl} = 6$, $k_0a = 10.1$ (c) $m_{cyl} = 8$, $k_0a = 13.6$ (d) $m_{cyl} = 11$, $k_0a = 18.9$.

constant but the sample spacing h (and consequently the cylinder radius is not strictly constant because m_{cyl} was also held constant within a single plot), convergence for a −5-percent speed-of-sound mismatch is possible for ϵ above 1.0 but not for ϵ below 1.0. Note that for $\epsilon \cong 0.8 - 0.9$, the aliasing is so great that the cylinder shape is almost lost in the reconstruction, while for ϵ greater than 1.0, the reconstructions all follow the cylinder shape and values fairly well. This being true for three different object sizes and grid sizes, as demonstrated in Fig. 7, gives substantial credibility to the Nyquist rate defined in Section IIID. It should be stressed that the four problems being solved within one plot are not exactly the same; that is, as h varies (m_{cyl} constant) the cylinder radius varies. This was unavoidable for the 11 × 11 grid. But the important point is that we are examining convergence for (similar) situations for which $h \cong \lambda/2, \lambda/2.5, \lambda/4$, and $\lambda/6.5$. Table IV summarizes this sampling rate study. Similar information is provided to that in the other tables except that here the first columns are λ/h, ϵ, and k_0a. Of special interest here is the huge increase in improvement factor between the runs with ϵ less than 1 and greater than 1, for all grid sizes (and radii).

Holding the radius constant at 0.9λ was tried for the 25 × 25 case. The experimental result for increasing the sampling rate from 1.4 to 2.1 times the Nyquist rate (and

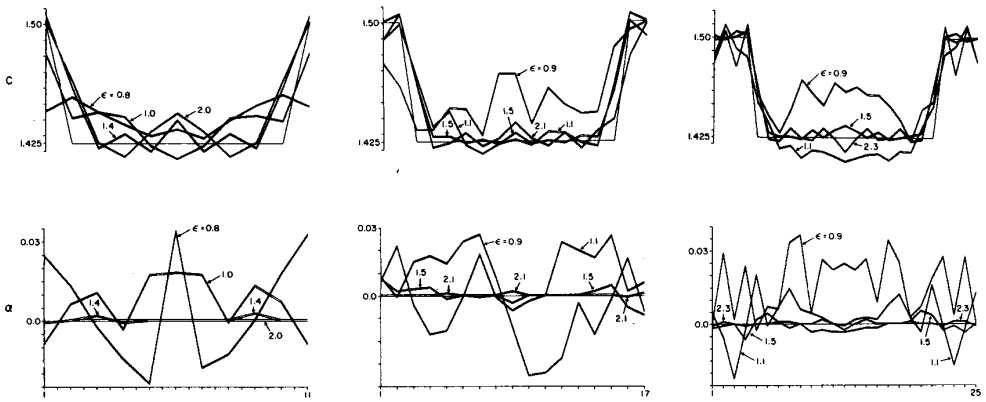

Fig. 7. Lossless circular cylindrical object reconstructions after four iterations. Dependence of reconstruction quality of speed of sound (above, mm/μsec) and adsorption (below, rad/mm) on sample spacing is shown for three object (and grid) sizes. Object contrast = -5 percent, $m_{cyl} = 2/3 \cdot (n_{max}/2 + 1)$, freq. = 2 MHz, sampling rates covering the range $\epsilon = 0.8$ to 2.3 are indicated by arrows on a single graph. Exact solution is lighter line. (a) $m_{cyl} = 4$, $n_{max} = 11$, $k_0 a = 5.8$. (b) $m_{cyl} = 6$, $n_{max} = 17$, $k_0 a = 9.7$. (c) $m_{cyl} = 8$, $n_{max} = 25$, $k_0 a = 13.6$.

TABLE IV
CHARACTERISTICS OF COMPUTER SIMULATION OF RECONSTRUCTION OF CIRCULAR CYLINDERS. SAMPLING RATES [OBJECT CONTRAST = -5 PERCENT, $m_{cyl} = 2/3(n^{max} + 1)$].

				Sum of squares of $\tilde{\gamma}_j - \gamma_j$			iter 4	iter 0	$\bar{c}_1$ Error
	λ/h	ϵ	$k_0 a$	iter 0	iter 1	iter 4	$n_{\gamma \neq 0}$	iter 4	(percent)
11×11	1.5	0.64	16.6	2700	2060	2130	45.3	1.27	2.9
$m_{cyl} = 4$	2.0	0.81	12.4	2700	1300	1000	21.	2.7	1.25
$n_{\gamma \neq 0} = 47$	2.5	0.95	9.94	2700	1220	580	12.3	4.7	0.86
$\|\gamma\|^2/n_{\gamma \neq 0} = 57.4$	4.3	1.42	5.78	2700	560	190	4.0	14.2	-0.004
	7.8	1.98	3.18	2700	370	250	5.3	10.8	-0.031
17×17	2.0	0.86	18.7	6500	4560	2654	23.9	2.45	1.63
$m_{cyl} = 6$	2.5	1.04	14.9	6380	3440	724	6.52	8.81	0.174
$n_{\gamma \neq 0} = 111$	3.85	1.47	9.6	6380	1960	330	3.0	19.3	0.084
$\|\gamma\|^2/n_{\gamma \neq 0} = 57.5$	6.44	2.11	5.8	6270	1010	340	3.06	18.4	0.026
25×25	2.0	0.90	24.9	11330	10470	6290	32.	1.8	2.68
$m_{cyl} = 8$	2.5	1.09	19.9	11210	8430	1440	7.3	7.8	-0.35
$n_{\gamma \neq 0} = 197$	3.7	1.51	13.6	11330	5040	520	2.64	21.8	0.09
$\|\gamma\|^2/n_{\gamma \neq 0} = 57.1$	4.8	1.85	10.5	11210	3470	460	2.34	24.4	0.086
	5.9	2.31	7.7	11210	2340	490	2.49	22.9	0.046

[a] Parameter varied: h (sampling rate). See text for definition of all parameters.

therefore m_{cyl} increased from 4 to 6) was that while there is an order of magnitude of improvement in the average value of the reconstructed speed of sound within the cylinder, c_1, (from -0.05-percent error to -0.005-percent error) the sum of squares of $\tilde{\gamma}_j - \gamma_j^{exact}$ relative to the number of pixels within the cylinder decreased only slightly. Of course, the improvement in c_1 may be in part due to the increased number of averaged points within the cylinder. That continuing to increase the sampling rate produces diminishing returns or even degradation (examine the column "(iter 4)/$n_{\gamma \neq 0}$" in Table IV) may stem from the various reconstruction equations being "too close" to each other, resulting in numerical problems [7], [2]. Further experimentation concerning this topic really requires larger n_{max} (grid sizes) but at present the algorithm is too slow to go much beyond 25×25 on our computer.

F. Iteration Duration

It is stated in [4] that about 3 or 4 runs through the equations (e.g. (5) and (6)) for the case of complete X-ray projections were needed for convergence. This idea was tried in the present implementation. Indeed, the error $\| f^{sc} - \Sigma D \gamma f \|^2$ in (5) decreased for a particular complete iteration if more runs through the equations were allowed. However, two points should be raised. First, the scattered field estimation error for any given iteration is not the one we wish to minimize. We wish to minimize

$\|\gamma - \gamma^{\text{exact}}\|^2$ over a series of iterations. Hence we are wasting time by trying to make a particular estimate of f^{sc} "too good" at any given point in the reconstruction process. Also, in ART, an example of a "row-action" method, only one row of the relevant matrix is held in memory at a time. But if further (more than one) runs through the equations are desired per iteration, the matrix elements must be recomputed (or else re-read in), which takes large amounts of time and only achieves small refinements on the estimate of only one of the two unknowns. Four runs through (5) and five runs through (6) per iteration were used over four complete iterations. The results were essentially the same as for the situation of only one run through each of (5) and (6) per iteration used over four iterations. This is true even though within each iteration, $\|f^{sc} - \Sigma D\gamma f\|^2$ was substantially smaller in the former case than in the latter.

G. Relaxation Parameters

The parameters β_0 and β_1 in (15) and (14), respectively, scale the correction made on the relevant unknown. They were held constant because the number of iterations was only four. In iterative numerical studies, such parameters must be determined by a search method; that is, trial and error. An example of this type of search is illustrated in Fig. 8, where the error $(1/n_{\gamma\neq 0})\|\tilde{\gamma} - \gamma^{\text{ex}}\|^2$ vs. β_1 is plotted for several trial runs. In this case the optimum β_1 is 0.23; however, the curve is somewhat problem-dependent. Fig. 8 was obtained for a -10-percent contrast object with $n_{\max} = 11$. For a 10-percent contrast object the optimal value of β_1 shifts to about 0.29, so an average between the two would be used in practice.

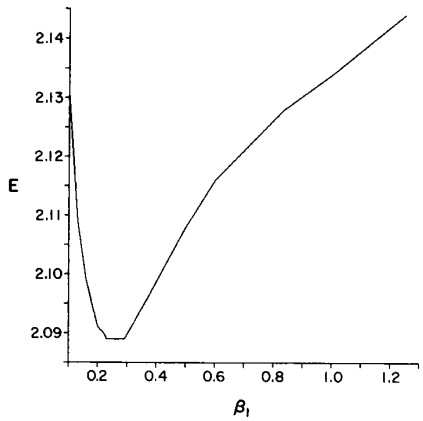

Fig. 8. Plot of log of normalized reconstruction error (sum of squares of $\tilde{\gamma}_j - \gamma_j^{\text{ex}}$ divided by $n_{\gamma\neq 0}$), E, after one iteration vs. relaxation constant β_1.

H. Execution Time

Taking these programming considerations into account, the tomography programs were run for four iterations. A marked improvement is apparent from iteration 1 to iteration 5. In this study, continuing the iterations beyond four had the effect of either minor improvement on the converging reconstructions or further deterioration in the diverging reconstructions. The execution times for 11×11, 17×17, and 25×25 grid sizes were, respectively, 5 min, 43 min, and 4.5 hours on our computer (VAX 11/730). The relation between these times follows almost exactly $n_{\max}^5$, as predicted in [5]. Though there are ways in which execution times could be reduced using further program optimization, the $n_{\max}^5$ relation (order of number of arithmetic operations per iteration) still holds and is the most serious limitation of the present algorithm in terms of its practical utility.

VI. Conclusion

The moment method presented by [5] and demonstrated here and in [12] has been shown to be a successful way to solve small inverse scattering problems of the type encountered in ultrasonic computed tomography. Not only is the method self-consistent (can go from γ^{exact} to scattered fields and back to $\tilde{\gamma} \cong \gamma^{\text{exact}}$) but it reconstructs circular cylinders equally well when given exact scattered field data. The main limitations of the algorithm are object contrast and execution time. For the former, [5] have presented alternative algorithms for solving (5) and (6) for γ. For the latter, [6] has proposed a modification to the present algorithm which is claimed to have a number of operations dependence of $n_{\max}^3 \log (n_{\max})$. Further investigation of these algorithms appears warranted, as it might bring the applicability of this method into the realm of real-world medical imaging.

References

[1] T. J. Cavicchi and W. D. O'Brien, "Heating distribution color graphics for homogeneous lossy spheres irradiated with plane wave ultrasound," *IEEE Trans. Sonics Ultrason.*, vol. 32, no. 1, pp. 17-25, Jan. 1985.

[2] M. P. Ekstrom, "A spectral characterization of the ill-conditioning in numerical deconvolution," *IEEE Trans. Audio Electroacoust.*, vol. 21, no. 4, pp. 344-348, Aug. 1973.

[3] G. T. Herman, A. Lent, and S. W. Rowland, "ART: Mathematics and applications," *J. Theor. Biol.*, vol. 42, no. 1, pp. 1-32, Nov. 1973.

[4] G. T. Herman, "A relaxation method for reconstructing objects from noisy x-rays," *Math. Prog.*, vol. 8, no. 1, pp. 1-19, Feb. 1975.

[5] S. A. Johnson and M. L. Tracy, "Inverse scattering solutions by a sinc basis, multiple source moment method—Part I: Theory," *Ultrason. Imaging*, vol. 5, pp. 361-375, 1983.

[6] S. A. Johnson, Y. Zhou, M. K. Tracy, M. J. Berggren, F. Stenger, "Inverse scattering solutions by a sinc basis, multiple source moment method—Part III: Fast algorithms," *Ultrason. Imaging*, vol. 6, pp. 103-116, 1984.

[7] V. G. Kogan, E. F. Lopes, "On the Born approximation for weak uniform scatterers," *Inverse Problems*, vol. 1, no. 4, pp 331-338, Nov. 1985.

[8] J. McNamee, F. Stenger, and E. L. Whitney, "Whittaker's Cardinal function in retrospect," *Math. Comput.*, vol. 25, no. 113, pp. 141-154, Jan. 1971.

[9] N. Mott and H. S. W. Massey, *The Theory of Atomic Collisions*, third edition. London: Oxford Univ. Press, 1965, p. 83.

[10] M. Slaney and A. C. Kak, "Imaging with diffraction tomography," Purdue University Technical Report TR-EE 85-5, 1985.

[11] M. Soumekh and M. Kaveh, "A theoretical study of model approx-

imation error in diffraction tomography," *IEEE Trans. Ultrason. Ferroelect. Freq. Contr.*, vol. 33, no. 1, pp. 10-20, Jan. 1986.

[12] M. L. Tracy and S.A. Johnson, "Inverse scattering solutions by a sinc basis, multiple source moment method—part II: numerical evaluations," *Ultrason. Imaging*, vol. 5, pp. 376-393, 1983.

Thomas J. Cavicchi was born in Cleveland, OH, in 1960. He received the B.S. degree in electrical engineering in 1982 from the Massachusetts Institute of Technology, and the M.S. degree in electrical engineering in 1984 from the University of Illinois, Urbana.

Since 1982 he has worked in the Bioacoustics Research Laboratory, Dept. of Electrical and Computer Engineering, at University of Illinois. He is currently studying inverse scattering in biological media.

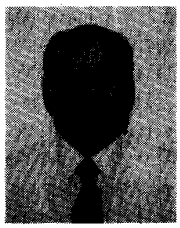

Steven A. Johnson was born in Preston, ID, on Jan. 13, 1939. He received the B.S. degree in Physics from Utah State University, Logan, UT, in 1961, and the M.S. degree in Physics from Stanford University, Stanford, CA, in 1967, and the Ph.D. degree in Physics from Stanford University, Stanford, CA, in 1971. From 1970 to 1979 he conducted x-ray and ultrasound research at the Mayo Clinic. Since then, while filling Professorial posts in the Departments of Bioengineering, Electrical Engineering, and Radiology, at the University of Utah in Salt Lake City, he has been engaged in research on ultrasound imaging using synthetic aperture and inverse-scattering techniques.

William D. O'Brien, Jr. (S'64-M'70-SM'79) was born in Chicago, IL, on July 19, 1942. He received the B.S., M.S., and Ph.D. degrees from the University of Illinois at Urbana-Champaign in 1966, 1968, and 1970, respectively.

From 1971-1975 he was with the Bureau of Radiological Health (currently the Center for Devices and Radiological Health) of the U.S. Food and Drug Administration, where he was the program project officer for the ultrasonic bioeffects area. From 1975-1987 he was an Assistant and Associate Professor, and since 1987 he has been a Professor of Electrical and Computer Engineering and of Bioengineering at the University of Illinois at Urbana-Champaign. He is also a member of the Radiation Oncology Traningship Faculty, the Nutritional Sciences Faulty, and the School of Basic Medical Sciences Faculty. He spent the academic year (1983-1984) on sabbatical leave at the University of Oxford in England. He has been a Visiting Scientist at the Mayo Clinic (1979), the AIUM representative to the task force in Geneva for the WHO publication *Environmental Health Criteria on Ultrasound* (1981), and a member of the National Institutes of Health Consensus Development Conference on Ultrasound Imaging in Pregnancy Panel (1983-1984).

His research interests involve the many areas of ultrasound-tissue interaction including spectroscopy, risk assessment, biological effects, tissue characterization, dosimetry, and acoustic microscopy, for which he has published over 70 papers. He is Editor in Chief of this TRANSACTIONS and also Associate Editor for biological and medical applications.

Dr. O'Brien is a fellow of the Acoustical Society of America and the American Institute of Ultrasound in Medicine and is a member of the American Association for the Advancement of Sciences, Sigma Xi, and Eta Kappa Nu. He is the recipient of an IEEE Centennial Medal (1984) and the AIUM Presidential Recognition Award (1985). He has been Secretary-Treasurer (1972-1980), Vice President (1981) and President (1982-1983) of the IEEE Sonics and Ultrasonics Group (currently the IEEE Ultrasonics, Ferroelectronics, and Frequency Control Society), was the Co-Chairman of the 1981 IEEE Ultrasonics Symposium and is the General Chairman of the 1988 IEEE Ultrasonics Symposium. Within AIUM he has been a member since 1974 and chairman (1979-1981) of its Bioeffects Committee, a member of the Board of Governors (1979-1985) and the AIUM Treasurer (1982-1985). He is currently AIUM's President-Elect (1986-1988). He was also the Co-Chairman of the task group which developed the AIUM/NEMA Safety Standard for Diagnostic Ultrasound Equipment (1976-1981). He is on the Editorial Boards of *Journal of Ultrasound in Medicine*, *Journal of Cardiovascular Ultrasonography*, and *Journal of Diagnostic Medical Sonography*.